University of Reading

Using the cold plasma dispersion relation and whistler mode waves to quantify the antenna sheath impedance of the Van Allen Probes EFW instrument

Article

Published Version

Hartley, D. P., Kletzing, C. A., Kurth, W. S., Bounds, S. R., Averkamp, T. F., Hospodarsky, G. B., Wygant, J. R., Bonnell, J. W., Santolik, O. and Watt, C. E. J. (2016) Using the cold plasma dispersion relation and whistler mode waves to quantify the antenna sheath impedance of the Van Allen Probes EFW instrument. Journal of Geophysical Research: Space Physics, 121 (5). pp. 4590-4606. ISSN 2169-9402 doi: 10.1002/2016JA022501 Available at https://centaur.reading.ac.uk/66094/

It is advisable to refer to the publisher's version if you intend to cite from the work. See Guidance on citing.

To link to this article DOI: http://dx.doi.org/10.1002/2016JA022501

Publisher: American Geophysical Union

All outputs in CentAUR are protected by Intellectual Property Rights law, including copyright law. Copyright and IPR is retained by the creators or other

University of Reading

copyright holders. Terms and conditions for use of this material are defined in the End User Agreement.

www.reading.ac.uk/centaur

CentAUR

Central Archive at the University of Reading

Reading's research outputs online

AGU PUBLICATIONS

JGR

Journal of Geophysical Research: Space Physics

RESEARCH ARTICLE

10.1002/2016JA022501

Key Points:
- Whistler mode wave power is compared to that calculated assuming cold plasma theory and including wave normal angle
- Structure of discrepancies consistent with variable sheath impedance between EFW electric field antenna and plasma
- Sheath impedance model is developed and shown to be successful in quantifying sheath impedance of EFW instrument

Correspondence to:
D. P. Hartley,
david-hartley@uiowa.edu

Citation:
Hartley, D. P., C. A. Kletzing, W. S. Kurth, S. R. Bounds, T. F. Averkamp, G. B. Hospodarsky, J. R. Wygant, J. W. Bonnell, O. Santolík, and C. E. J. Watt (2016), Using the cold plasma dispersion relation and whistler mode waves to quantify the antenna sheath impedance of the Van Allen Probes EFW instrument, *J. Geophys. Res. Space Physics*, *121*, 4590–4606, doi:10.1002/2016JA022501.

Received 5 FEB 2016
Accepted 9 MAY 2016
Accepted article online 14 MAY 2016
Published online 31 MAY 2016

©2016. American Geophysical Union. All Rights Reserved.

Using the cold plasma dispersion relation and whistler mode waves to quantify the antenna sheath impedance of the Van Allen Probes EFW instrument

D. P. Hartley[1], C. A. Kletzing[1], W. S. Kurth[1], S. R. Bounds[1], T. F. Averkamp[1], G. B. Hospodarsky[1], J. R. Wygant[2], J. W. Bonnell[3], O. Santolík[4,5], and C. E. J. Watt[6]

[1]Department of Physics and Astronomy, University of Iowa, Iowa City, Iowa, USA, [2]School of Physics and Astronomy, University of Minnesota, Twin Cities, Minneapolis, Minnesota, USA, [3]Space Sciences Laboratory, University of California, Berkeley, California, USA, [4]Department of Space Physics, Institute of Atmospheric Physics, Prague, Czech Republic, [5]Faculty of Mathematics and Physics, Charles University, Prague, Czech Republic, [6]Department of Meteorology, University of Reading, Reading, UK

Abstract Cold plasma theory and parallel wave propagation are often assumed when approximating the whistler mode magnetic field wave power from electric field observations. The current study is the first to include the wave normal angle from the Electric and Magnetic Field Instrument Suite and Integrated Science package on board the Van Allen Probes in the conversion factor, thus allowing for the accuracy of these assumptions to be quantified. Results indicate that removing the assumption of parallel propagation does not significantly affect calculated plasmaspheric hiss wave powers. Hence, the assumption of parallel propagation is valid. For chorus waves, inclusion of the wave normal angle in the conversion factor leads to significant alterations in the distribution of wave power ratios (observed/ calculated); the percentage of overestimates decreases, the percentage of underestimates increases, and the spread of values is significantly reduced. Calculated plasmaspheric hiss wave powers are, on average, a good estimate of those observed, whereas calculated chorus wave powers are persistently and systematically underestimated. Investigation of wave power ratios (observed/calculated), as a function of frequency and plasma density, reveals a structure consistent with signal attenuation via the formation of a plasma sheath around the Electric Field and Waves spherical double probes instrument. A simple, density-dependent model is developed in order to quantify this effect of variable impedance between the electric field antenna and the plasma interface. This sheath impedance model is then demonstrated to be successful in significantly improving agreement between calculated and observed power spectra and wave powers.

1. Introduction

The outer electron radiation belt is highly dynamic in space and time, particularly during periods of enhanced geomagnetic activity [e.g., *Onsager et al.*, 2002; *Reeves et al.*, 2003; *Green et al.*, 2004; *Morley et al.*, 2010; *Turner et al.*, 2012; *Hartley et al.*, 2013, 2014]. This variability is, in part, driven by wave-particle resonance with whistler mode waves (e.g., chorus [*Horne and Thorne*, 1998; *Summers et al.*, 2002] and plasmaspheric hiss [*Meredith et al.*, 2007; *Summers et al.*, 2008]). Occuring in the $0.1f_{ce}$ to $0.9f_{ce}$ frequency range, where f_{ce} is the electron gyrofrequency, chorus waves typically exhibit a two-band structure, lower and upper, separated by a characteristic minimum in spectral density at $0.5f_{ce}$ [e.g., *Tsurutani and Smith*, 1974; *Meredith et al.*, 2012; *Li et al.*, 2013; *Fu et al.*, 2015]. Whistler mode chorus waves are typically observed in the low-density region outside of the plasmasphere [*Burtis and Helliwell*, 1969; *Tsurutani and Smith*, 1977] and are considered to be highly efficient for the local acceleration of electrons in the radiation belt region [*Summers et al.*, 1998; *Thorne*, 2010]. Recent observations of phase space density maxima within the outer radiation belt region [e.g., *Green and Kivelson*, 2004; *Chen et al.*, 2007; *Turner et al.*, 2010; *Shprits et al.*, 2012; *Reeves et al.*, 2013] indicate the importance of local acceleration by chorus waves.

Plasmaspheric hiss (100 Hz $< f <$ ~5 kHz) is a broadband, whistler mode emission that is confined to the higher-density plasmasphere and can drive pitch angle scattering of radiation belt electrons, resulting in losses to the atmosphere as electrons populate the bounce loss cone. This scattering has shown to play an important role in the formation of the slot region [e.g., *Lyons et al.*, 1972; *Lyons and Thorne*, 1973] as well as contributing to the quiet time decay of the outer electron radiation belt [e.g., *Summers et al.*,

2007; *Lam et al.*, 2007; *Thorne et al.*, 2013]. Hence, in order to completely understand radiation belt dynamics, it is crucial to correctly model these whistler mode waves and their interactions with radiation belt particles.

Energy and pitch angle diffusion rates scale with the magnetic field wave power [*Kennel and Engelmann*, 1966; *Summers and Ma*, 2000]. As such, this quantity has been the subject of numerous previous studies [e.g., *Meredith et al.*, 2003a, 2003b, 2004; *Horne et al.*, 2005; *Meredith et al.*, 2012]. When the magnetic wave field is not directly measured, the assumptions of cold plasma theory and parallel wave propagation are often used to infer the magnetic wave power from electric field observations. However, observations indicate that for chorus waves at low latitudes, the wave vector may not always be directed near parallel to the background magnetic field [*Santolik et al.*, 2009, 2014a]. In the curved magnetic field of the magnetosphere, refraction is predicted to quickly increase wave angles away from the field-aligned direction [*Watt et al.*, 2012]. Nevertheless, observations show that the wave vector directions of intense chorus waves are close to a Gaussian-shaped peak centered about the local magnetic field direction. The width of this peak is between 10° and 20°. However, a fraction of oblique waves still exists [*Santolík et al.*, 2014b]. As such, calculated wave powers that assume parallel propagation may not always be accurate [e.g., *Hartley et al.*, 2015]. The comprehensive in situ observations available from the Van Allen Probes spacecraft allow for these assumptions (i.e., cold plasma theory and parallel wave propagation) to be tested thoroughly. In this study, discrepancies between observed and calculated whistler mode power spectra and wave power are investigated as functions of measured frequency range and plasma density, with instrument-plasma coupling effects identified, modeled, and corrected for. This study aims to take steps toward determining the appropriate theoretical treatment of whistler mode waves (i.e., testing the validity of cold plasma theory in plasma containing significant warm/hot component), to determine the accuracy of assumptions implemented in previous studies (i.e., parallel wave propagation), and to quantify the effect of instrument-plasma coupling on the electric field output from the Van Allen Probes Electric Field and Waves Instrument (EFW) [*Wygant et al.*, 2013].

2. Cold Plasma Dispersion Relation

The Electric and Magnetic Field Instrument Suite and Integrated Science (EMFISIS) instrument suite [*Kletzing*, 2013] measures both electric and magnetic field power spectra over both the plasmspheric hiss and chorus wave frequency ranges at 6 s time resolution. By comparing the measured magnetic field wave power with that calculated using the measured electric field (both by assuming parallel propagation and then by considering the wave normal angle), the accuracy of the cold plasma assumption, in addition to the assumption of parallel wave propagation, can be explored.

In order to calculate chorus wave powers, the observed and calculated magnetic field power spectra are integrated across the 0.1 – 0.9 f_{ce} frequency range, with no consideration of their particular time-frequency structure. For plasmaspherc hiss the frequency range is 100 Hz to 5 kHz. Since the frequency range of chorus waves and plasmaspheric hiss may overlap, a density criterion is employed in order to distinguish between the two. To be classified as chorus (plasmaspheric hiss), the spacecraft are required to be outside (inside) of the plasmasphere. Observations are considered to be outside of the plasmasphere if the plasma density is less than $10 \times (6.6/\mathrm{L})^4$ or 30 cm^{-3} (whichever is smaller) [*Li et al.*, 2014]. Conversely, data are considered to be inside of the plasmasphere if the plasma density is greater than $10 \times (6.6/\mathrm{L})^4$ or 30 cm^{-3} (whichever is greater). Additional filtering is performed in order to isolate whistler mode waves with a well-defined wave vector direction. In order to be considered as whistler mode, and therefore included in this study, the planarity of magnetic field polarization [*Santolík et al.*, 2003, equation (12)], the ellipticity of magnetic field polarization [*Santolík et al.*, 2003, equation (13)], and the degree of magnetic field polarization in the polarization plane [*Santolík et al.*, 2002, equation (A6)] must all be greater than 0.5. The planarity filter is introduced to ensure that the plane wave assumption is valid. The polarization and ellipticity provide information on the wave coherence and on the ratio of the two axes of the polarization ellipse, hence, only including data where both of these parameters are greater than 0.5 ensures that the wave polarization is coherent, near circular and right handed. Additionally, periods of shadow on the spin-axis electric field sensor, eclipse periods, spacecraft charging events, and maneuver periods are removed from the data set.

Initially, the criteria for isolating whistler mode waves are tested for a sample time period where plasmaspheric hiss and chorus waves are both observable in the wave power spectra from EMFISIS. Figure 1 shows L shell and plasma density, the electric (S_E) and magnetic (S_B) wave spectral powers (sum of all three

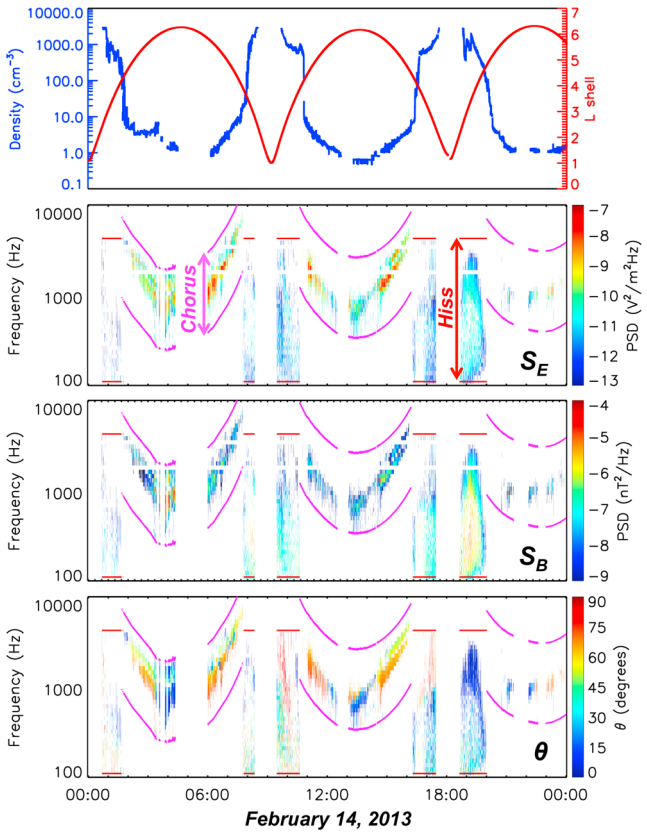

Figure 1. A survey plot of the L shell (red) and plasma density (blue), electric (S_E) and magnetic (S_B) wave spectral powers, in addition to the wave normal angle, θ, observed by Van Allen Probe A on 14 February 2013. The pink lines indicate 0.1 and 0.9 f_{ce} where the density criteria for chorus are met and f_{pe} data are available. The red lines indicate 100 Hz and 5 kHz where the density criteria for plasmaspheric hiss are met and f_{pe} data are available.

components, background subtracted), in addition to the wave normal angle, θ, from Van Allen Probe A on 14 February 2013. Note that the wave normal angle is defined as the angle between the wave vector, k, and the the background magnetic field vector. The pink lines indicate 0.1 and 0.9 f_{ce} where the criteria for observations to be identified as chorus waves are met and f_{pe} data are available. The red lines indicate 100 Hz and 5 kHz where the criteria for observations to be identified as plasmaspheric hiss are met and f_{pe} data are available. Data are not included if the planarity, ellipticity, and polarization criteria are not met. The data gaps at perigee (low L shell) are due to the upper hybrid line exceeding the upper limit of the EMFISIS frequency range; hence, the upper hybrid frequency cannot be identified, and the density cannot be determined. This occurs frequently during the mission (approximately 2 h each day). From Figure 1, it is apparent that the employed criteria are successful in isolating whistler mode chorus waves and plasmaspheric hiss. Chorus waves are observable between ~2 and 8 UT and between ~11 and 16 UT, where the spacecraft is identified as outside of the plasmasphere. During the period of most intense chorus activity (centered around 4 UT), the wave normal angles are small (blue colors), and hence, the direction of propagation is near parallel with respect to the background magnetic field. However, during less intense chorus activity, the wave normal angles are larger (more oblique propagation). Plasmaspheric hiss is observable when the spacecraft is identified to be inside of the plasmasphere (between ~8 and 11 UT and between ~15 and 20 UT). During the intense period of plasmapsheric hiss observable between ~19 and 20 UT, the wave normal angle is approximately field aligned. The data gaps indicate periods where the plasma frequency inferred from the upper hybrid line is not available.

The conversion from electric to magnetic field power spectra, assuming a cold plasma dispersion relation and parallel wave propagation, may be performed using

$$S_B = \frac{1}{c^2}\left(1 - \frac{f_{pe}^2}{f\left(f - f_{ce}\right)}\right) S_E \tag{1}$$

where S_B and S_E are the magnetic and electric field spectral powers respectively, c is the speed of light, f is the wave frequency, f_{pe} is the electron plasma frequency, and f_{ce} is the electron gyrofrequency [*Meredith et al.*, 2004]. (Note that in this study, only electron terms are considered (ion terms neglected), and f_{ce} is defined as $|q|B/m$, neglecting the charge sign.)

The electron gyrofrequency is determined using the Van Allen Probes EMFISIS magnetometer instrument, and the plasma frequency, f_{pe}, is inferred from the upper hybrid line [*Kurth et al.*, 2015]. With current empirical wave models [e.g., *Meredith et al.*, 2003a, 2004, 2012] as well as diffusion coefficients and acceleration timescales [e.g., *Horne et al.*, 2005], based on wave powers calculated using this equation, it is crucial to explore the validity of the embedded assumptions.

The wave normal angle is routinely calculated from the EMFISIS magnetic field data using the singular value decomposition method [*Santolík et al.*, 2003], thus allowing for the assumption of parallel wave propagation to be removed. To quantify the effect of including the measured angle of propagation in converting between electric and magnetic field power spectra, equation (1) is modified in order to include the wave normal angle, yielding

$$S_B = \frac{n^2}{c^2}\left(\frac{\left(\frac{D}{S-n^2}\right)^2\left(P-n^2\sin^2\theta\right)^2 + P^2\cos^2\theta}{\left(P-n^2\sin^2\theta\right)^2\left[\left(\frac{D}{S-n^2}\right)^2+1\right] + (n^2\cos\theta\sin\theta)^2}\right)S_E \tag{2}$$

where n is the refractive index (see equation (3)), θ is the wave normal angle, and R, L, P, D, and S are the Stix parameters [*Stix*, 1992] (calculated using equations (4)–(8)).

$$n^2 = \frac{RL\sin^2\theta + PS(1+\cos^2\theta) - \sqrt{(RL-PS)^2\sin^4\theta + 4P^2D^2\cos^2\theta}}{2\left(S\sin^2\theta + P\cos^2\theta\right)} \tag{3}$$

$$R = 1 - \frac{f_{pe}^2}{f(f-f_{ce})} \tag{4}$$

$$L = 1 - \frac{f_{pe}^2}{f(f+f_{ce})} \tag{5}$$

$$P = 1 - \frac{f_{pe}^2}{f^2} \tag{6}$$

$$D = \frac{1}{2}(R-L) \tag{7}$$

$$S = \frac{1}{2}(R+L) \tag{8}$$

The instrument background levels are subtracted from the observed electric and magnetic field spectral powers in addition to the removal of two frequency bands at 1998 Hz (bandwidth of 231.7 Hz) and at 3988 Hz (bandwidth of 459.2 Hz) due to elevated noise levels in the electric field power spectra at these frequencies. The same frequency bands are removed from the magnetic field power spectra in order for the calculated integral wave powers to remain comparable. Removing these frequency bands certainly reduces the noise levels; however, noise may also be apparent in the surrounding frequency bands and as such, is not fully removed. Additionally, if the calculated spectral power is undefined at a specific frequency, the spectral power at this frequency is not included in the calculation of the observed integral wave power. When parallel propagation is assumed, there is no filter placed on the permitted range of wave normal angles. However, when the wave normal angle is considered in the calculation, data are removed if the wave normal angle is greater than either the resonance cone angle minus 5°, or 75°, whichever is smaller. This is done in order to ensure that magnetosonic waves are not included.

Hartley et al. [2015] used a 20 day sample of EMFISIS data from Van Allen Probe A to compare chorus wave powers calculated using equation (1) with those observed and concluded that during active conditions (observed chorus wave powers, $B_w^2 > 10^{-3}$ nT^2), calculated chorus wave powers were underestimated by a factor of 2, or greater, approximately 60% of the time. Additionally, during less active conditions (observed chorus wave powers, $B_w^2 < 10^{-3}$ nT^2), calculated chorus wave powers could be significantly greater than those observed. The cause of these discrepancies was attributed to either the assumption of a cold plasma regime or the assumption of parallel wave propagation. The current study goes much further than this preliminary work by investigating the effect including the wave normal angle in the calculation, as well as implementing significantly more data, 417 days of data from Van Allen Probe A and 172 days of data from Van Allen Probe B. Additionally, the current study employs a more rigorous filtering criteria in order to ensure only plane waves propagating in the whistler mode are included, as well as investigating and quantifying the effect of variable impedance between the electric field antenna and the plasma.

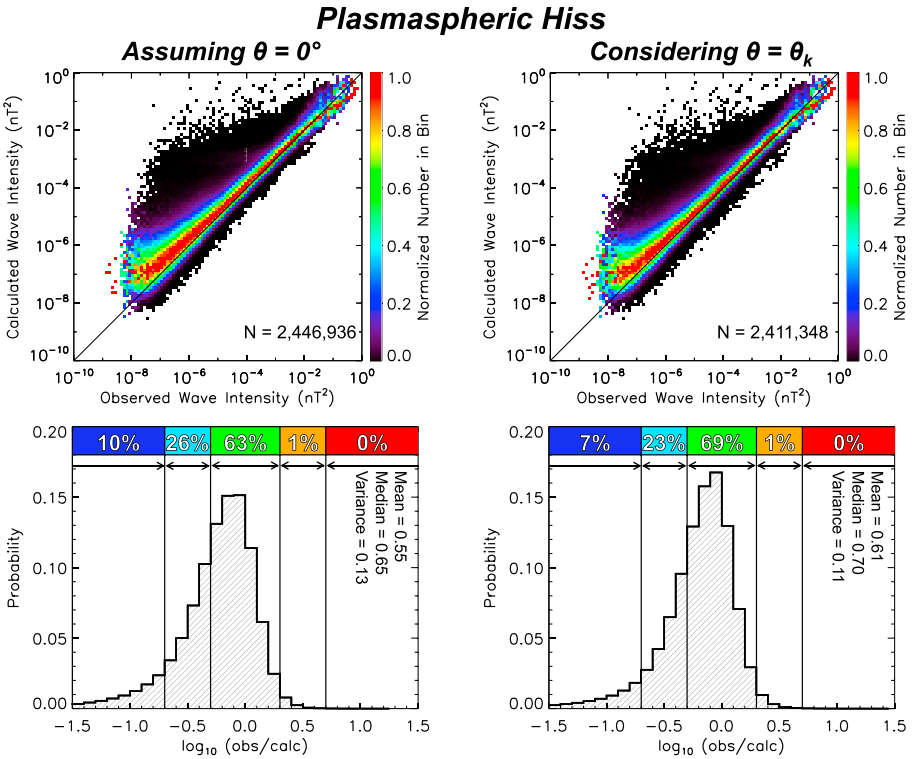

Figure 2. The distributions of observed and calculated plasmaspheric hiss wave powers as described in section 3.1.

3. Wave Power: Observed and Calculated

Plasmaspheric hiss and chorus wave powers are calculated for 589 satellite days of available spacecraft data to compare observed wave powers with those calculated using the cold plasma dispersion relation (firstly assuming parallel propagation and then considering the wave normal angle).

3.1. Plasmaspheric Hiss

Figure 2 (top row) contains direct comparisons between the observed wave power and the wave power calculated using the cold plasma dispersion relation assuming parallel propagation ($\theta = 0°$, top left) and considering the wave normal angle ($\theta = \theta_k$, top right) for plasmaspheric hiss. The color indicates the number of data in each bin, normalized to the maximum number of occurrences in each observed wave power column. If calculated wave powers were equal to those observed at each instance of time, all of the data would lie along the diagonal line of equivalence. The total number of occurrences, *N*, is also listed on the figure. Note that the difference in number of occurrences between figure panels is due to the removal of observations where the wave normal angle is close to, or within, the resonance cone.

Assuming parallel wave propagation (Figure 2, top left), the majority of data lies on, or slightly above, the line of equivalence. This indicates that assuming parallel propagation and a cold plasma dispersion relation yields, on average, accurate calculated magnetic wave powers for plasmaspheric hiss. Including the wave normal angle in the conversion factor (Figure 2, top right) has little impact on the calculated wave powers. This is due to the fact that the wave normal angle for plasmaspheric hiss is often very close to the field-aligned direction, and thus, the assumption of parallel propagation is often valid. To investigate the shape of the distribution of data about the line of equivalence, the ratio between the calculated and observed wave powers (observed/calculated) is computed for each time instance. These values are calculated in base 10 logarithm space so that ratios of 0.1 and 10 are considered to have the same deviation from a ratio of unity (−1.0 and 1.0 about a ratio of zero in logarithm space). Figure 2 (bottom row) contains probability distributions of the logarithm of the plasmaspheric hiss wave power ratio, assuming parallel propagation (Figure 2, bottom left), and considering the wave normal angle (Figure 2, bottom right). In order to quantify the accuracy of the calculated wave powers, the percentage of data in discreet ratio bins is computed. These ratio bins are parametrized as: calculated wave power is an overestimate by a factor greater than 5 (Ratio < 0.2, dark blue),

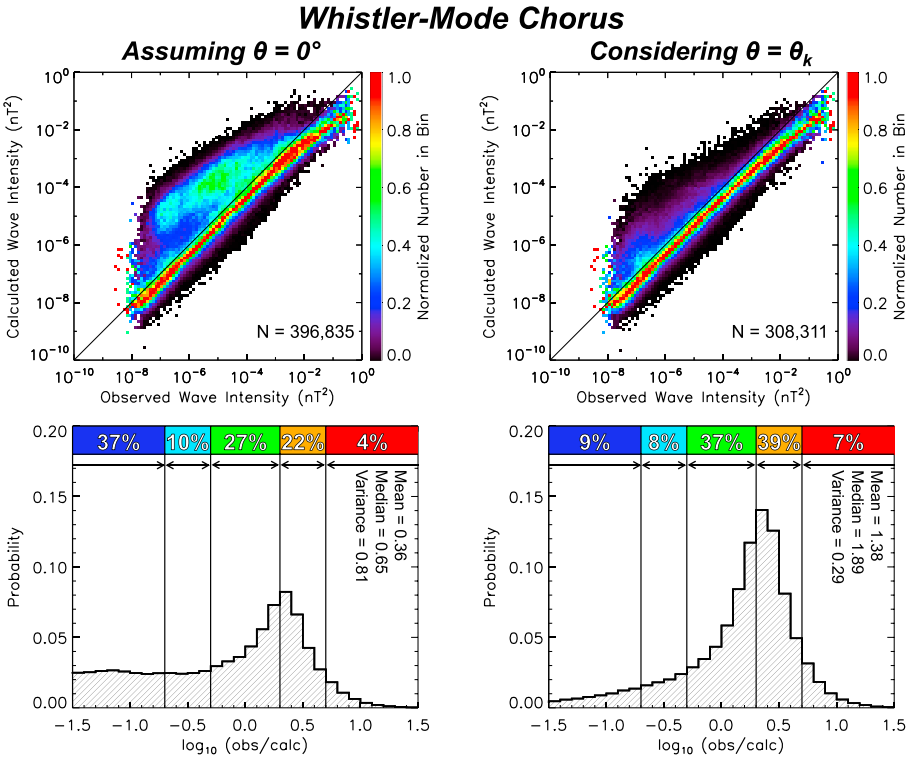

Figure 3. The same parameters as shown in Figure 2 for whistler mode chorus waves.

calculated wave power is an overestimate by a factor greater than 2 but less than 5 (0.2 < Ratio < 0.5, light blue), calculated wave power is within a factor of 2 of the observed value (0.5 < Ratio < 2.0, green), calculated wave power is an underestimate by a factor greater than 2 but less than 5 (2.0 < Ratio < 5.0, orange), and calculated wave power is an underestimate by a factor greater than 5 (Ratio > 5.0, red). The mean, median, and variance of the distributions are also listed on each panel. When parallel propagation is assumed (Figure 2, bottom left), the calculated wave power is within a factor of 2 of that observed for 63% of the period studied. Overestimates occur for 36% of the data (26% by a factor greater than 2 but less than 5, and 10% by a factor greater than 5), whereas underestimates rarely occur (only 1% of data). The inclusion of the wave normal angle (Figure 2 bottom right) slightly improves these values with the percentage of calculated wave powers that are within a factor of 2 of those observed increasing from 63% to 69%, and the percentage of overestimates decreasing from 36% to 30%. This improvement in agreement is also shown by the mean increasing from 0.55 to 0.61, the median increasing from 0.65 to 0.70, and the variance decreasing from 0.13 to 0.11. These results indicate that the assumption of parallel wave propagation is often valid for plasmaspheric hiss and that using the cold plasma dispersion relation and the measured electric field, on average, yields an accurate estimation of the magnetic field wave power for plasmaspheric hiss.

3.2. Chorus

Figure 3 displays the same parameters as Figure 2 but for whistler mode chorus waves instead of plasmaspheric hiss. When parallel propagation is assumed (Figure 3, top left), there are a substantial amount of data above the line of equivalence. In particular, there exists a population of data between observed wave powers of 10^{-7} and 10^{-4} nT^2 where the calculated wave powers are overestimated by an order of magnitude or greater. However, underestimates of the chorus wave power are also a common occurrence (data below the equivalence line) with the highest density of data (red bins) lying around a factor of 2 or 3 below the equivalence line. The inclusion of the wave normal angle (Figure 3, top right) in the conversion from electric to magnetic field power spectra significantly reduces the number of overestimates of calculated chorus wave power. This indicates that the angle of propagation for chorus waves is oblique in these cases; hence, the assumption of parallel propagation is not always valid. The remaining discrepancies appear to be better described as a systematic underestimate.

The distribution of data about the line of equivalence is investigated further, with Figure 3 (bottom row) containing probability distributions of the logarithm of the chorus wave power ratio assuming parallel propagation (Figure 3, bottom left) and considering the wave normal angle (Figure 3, bottom right). When parallel propagation is assumed, the calculated wave power is within a factor of 2 of that observed for 27% of the period studied, with overestimates occurring for 47% of the data (10% by a factor greater than 2 but less than 5, and 37% by a factor greater than 5). Despite the large number of overestimates, the peak of the distribution is centered between a ratio of 2 and 3 (0.3 to 0.5 on log scale). The variance of the log distribution is 0.81. When the wave normal angle is considered in the conversion from electric to magnetic field power spectra, the calculated chorus wave powers are more closely matched to those observed. The high volume of data observed above the line of equivalence, in addition to the large data spread, is significantly reduced (variance of log-ratio distribution reducing from 0.81 to 0.29). The percentage of overestimates by a factor greater than 5 reduces significantly from 37% to only 9%. The remaining discrepancies appear to be better described as a systematic offset of the ratio distribution that may be rectified by a constant multiplication factor. Given that the spread of the distribution significantly decreases by including the wave normal angle in the conversion factor, it is apparent that the angle of propagation is an important parameter to consider when dealing with chorus waves. That is, chorus waves are sometimes oblique; hence, the assumption of parallel propagation is not always valid. It is noted that these results are consistent with previous theoretical results [e.g., *Ni et al.*, 2011] who showed that removing the assumption of parallel propagation may only decrease calculated magnetic wave powers.

One cause of the remaining discrepancies is uncertainty in the plasma frequency; however, this is only between 10 and 20%. Errors of this magnitude would lead to a maximum error factor of 1.44 in the calculated wave powers (scatter about zero between −0.16 and 0.16 on log scale) and therefore cannot fully explain the observed deviations. Additionally, errors from this source would likely lead to scattering of the calculated wave powers around about the average value, not the systematic offset that is observed. Another possible cause of discrepancies is instrument-plasma coupling, which is discussed further in section 5.

Comparison between observed and calculated wave powers (considering the wave normal angle) for chorus waves and plasmaspheric hiss reveals one significant difference. That is, the calculated chorus wave powers are systematically underestimated by a factor of approximately 2 or 3; however, the plasmaspheric hiss wave powers are much more closely matched to those observed (slight overestimates). In order to investigate this difference, the observed and calculated power spectra are investigated as a function of plasma density and instrument frequency channels. From this point in the study, the calculated wave powers will always have the wave normal angle included in the conversion factor.

4. Density and Frequency Variations

Chorus waves and plasmaspheric hiss are both whistler mode emissions; however, they are distinguishable by their differences in (i) frequency range and (ii) background plasma density. In order to investigate these differences, data are binned in small intervals of plasma density and kept as a function of measured frequency channels. Figure 4 (left) shows the median of the logarithm of the wave power ratio distribution (observed/calculated) for each of these frequency and plasma density bins. The vertical dashed line indicates the imposed density criterion that is used to define the plasmapause in this study (separation between chorus waves and plasmaspheric hiss). Displaying data in this way allows for the identification of specific frequency and/or density bins which may be the root of why systematic underestimates of wave power are observed for chorus waves, but not for plasmaspheric hiss. For higher densities (greater than $\sim$ 20 cm^{-3}) and frequencies between 100 and 1000 Hz, calculated wave powers are typically accurate or slightly overestimated. For lower densities and higher frequencies, underestimates of wave power are typically observed. A feature that is apparent from Figure 4 (left) is the distinct boundary between accurate or small overestimates of wave power (white/blue) and underestimates of wave power (red) running diagonally upward in frequency with increasing density from $\sim$10 cm^{-3} at a frequency of 100 Hz, up to $\sim$1000 cm^{-3} at 2000 Hz. This boundary is highlighted on Figure 4 (left) by a dashed black diagonal line. For frequencies/densities to the right of this boundary the wave power is typically accurate or slightly overestimated. For frequencies/densities to the left of this boundary the wave power is typically underestimated. This is consistent with the integral wave powers shown in Figures 2 and 3.

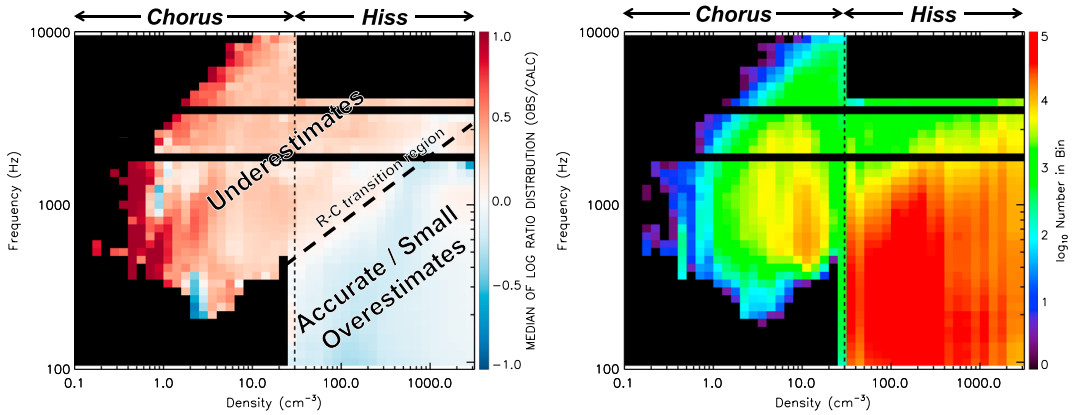

Figure 4. (left) The median of the logarithm of the wave power ratio distribution (observed/calculated) as a function of frequency channel and plasma density. The dashed vertical line indicates the plasmapause boundary between chorus waves and plasmaspheric hiss. The diagonal dashed line indicates the possible transition region from resistive to capacative plasma coupling. (right) The logarithm of the number of data in each density/frequency bin.

Figure 4 (right) shows the number of occurrences in each density/frequency bin. It is evident that the majority of plasmaspheric hiss waves occur between 100 and ~2000 Hz with very little dependence on density. In comparison, the majority of chorus waves occur at densities of ~10 cm^{-3} and frequencies between 500 and 4000 Hz. The number of data in each bin is important to consider when evaluating the statistical significance of the average wave power ratios shown in Figure 4 (left).

From Figure 4, the general structure of the discrepancies between observed and calculated whistler mode wave powers becomes apparent; underestimates become increasingly common at higher frequencies and lower densities. This structure lends itself to the possibility that instrument-plasma coupling effects with the EFW spherical double probes may be the cause of the observed underestimates, as is discussed subsequent sections.

5. Instrument-Plasma Coupling: Sheath Effects

The formation of a plasma sheath around the spherical double probes of the EFW instrument can attenuate the output voltage, leading to underestimates of the electric field wave power (and thus underestimates of the calculated magnetic field wave power). A simple method to model this effect, which works well under a broad range of plasma conditions [*Gurnett*, 1998], is to represent the coupling of the electric dipole antenna to the plasma by a voltage divider with complex impedance. The electric antenna of the EFW are considered to be connected to the plasma through the parallel combination of a resistor and a capacitor in the sheath region. Figure 5 shows the circuit diagram that is used to simulate these instrument-plasma coupling effects. The load resistance and capacitance of the EFW antenna are estimated to be 1 TOhm, and 7 pF, respectively.

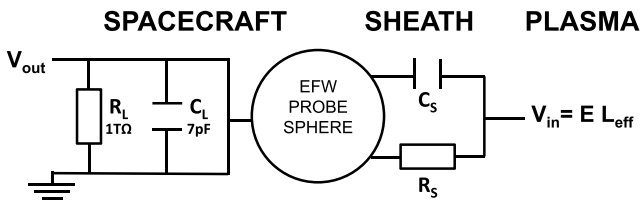

Figure 5. The voltage divider circuit used to represent the electric field antenna immersed in a plasma. R_S and C_S are the sheath resistance and capacitance respectively, whereas R_L and C_L are the load resistance and capacitance respectively.

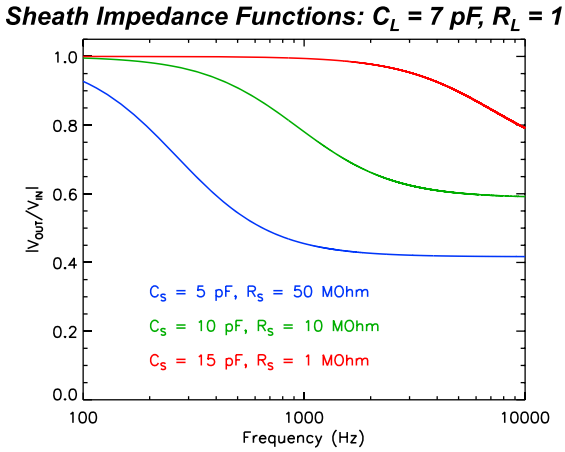

Figure 6. A plot showing the frequency dependence of equation (9) for three sample cases; R_S = 1, 10, and 50 MOhm and C_S = 15, 10, 5 pF (R_L = 1 TOhm, C_L = 7 pF). The blue line represents the sheath impedance function in a low-density plasma, the green line in a middle density plasma, and the red line in a high-density plasma.

This configuration yields the sheath impedance function (ratio of output voltage to input voltage):

$$\left|\frac{V_{\text{out}}}{V_{\text{in}}}\right| = \left|\frac{V_{\text{out}}}{EL_{\text{eff}}}\right| = \left[1+\frac{R_S}{R_L}\left(\frac{1+j\omega R_L C_L}{1+j\omega R_S C_S}\right)\right]^{-1} \tag{9}$$

where V_{in} and V_{out} are the input an output voltages respectively, E is the electric field, L_{eff} is the effective length (typically equal to the probe separation for spherical double probes), j is the imaginary unit, ω is the angular frequency ($2\pi f$), R_S and C_S are the sheath resistance and capacitance respectively, and R_L and C_L are the load resistance and capacitance respectively [e.g., *Boehm et al.*, 1994].

The form of this function is shown over the 100 Hz to 10 kHz frequency range in Figure 6 for three sample cases R_S = 1, 10, 50 MOhm, C_S = 15, 10, 5 pF, with R_L = 1 TOhm, and C_L = 7 pF (the load resistance and capacitance of the EFW probes). The region where the function rolls off is known as the RC transition frequency. Below this frequency resistive probe-plasma coupling dominates, whereas above this frequency capacitive probe-plasma coupling dominates. The sheath resistance is expected to decrease with increasing plasma density, whereas the sheath capacitance is expected to increase with increasing density. Hence, it may be considered from Figure 6, the blue line represents the sheath impedance function at low densities, the green line represents the sheath impedance function at middle densities, and the red line represents the sheath impedance function at high densities. These sheath impedance functions are consistent with the structure seen in Figure 4, with underestimates occurring only at higher frequencies at high density and spreading to lower frequencies with decreasing density. An estimate of the RC transition region is also labeled on Figure 4. It is therefore believed that instrument-plasma coupling effects are playing a role in causing the observed underestimates of wave powers calculated from electric field measurements.

Sheath impedance functions depend upon both the plasma side, and the antenna side, of the circuit (see Figure 5). Therefore, any differences between the antennas construction also lead to differences in the sheath impedance functions. The EFW instrument consists of two different antenna types, (i) centrifugally deployed wire booms in the spin plane with a tip-to-tip separation of ~100 m and (ii) rigid booms along the spin axis with a tip-to-tip separation of ~12–14 m. Apart from the separation distance, the main difference between the spin-plane and spin-axis sensors is that the spin-plane sensor elements have both a 4 cm radius sphere (~4 pF vacuum capacitance) and a 3 m long fine wire (~10 pF vacuum capacitance), whereas the spin-axis sensors just have the 4 cm radius spheres. Hence, the sheath capacitance values are different for the spin-plane and spin-axis antennas. The effective input capacitance of each antenna was estimated in ground calibration using a known parallel RC sheath simulator in series between the signal generator input and the sensor input with the partially deployed sensor and preamp in a Faraday Box (FBOX). Using measurements with a driven FBOX, and a grounded FBOX allowed for the effective input capacitance to be determined for each antenna (~7 pF for the spin plane, ~6 pF for the spin axis). Due to these differences, ideally, a different sheath impedance function would be applied to each of the EFW antenna types (one function to the spin plane antennas and one function to the spin axis antenna). However, a good approximation of the sheath impedance can be obtained by applying only one sheath impedance function to the sum of the outputs from all three antennas as indicated by Figure 7. Figure 7 (left) shows two different sheath impedance functions, one for approximated values of the spin plane antenna (R_L = 1 TOhm, R_S = 20 MOhm, C_L = 7 pF, and C_S = 14 pF) and one for approximated values of the spin axis antenna (R_L = 1 TOhm, R_S = 20 MOhm, C_L = 6 pF, and C_S = 7 pF). Figure 7 (right) shows how these individual sheath impedance functions would affect the total electric field (sum of all three components) assuming an equal contribution from each component (black line). The red line shows a single sheath impedance function (R_L = 1 TOhm and C_L = 7 pF) that is fitted

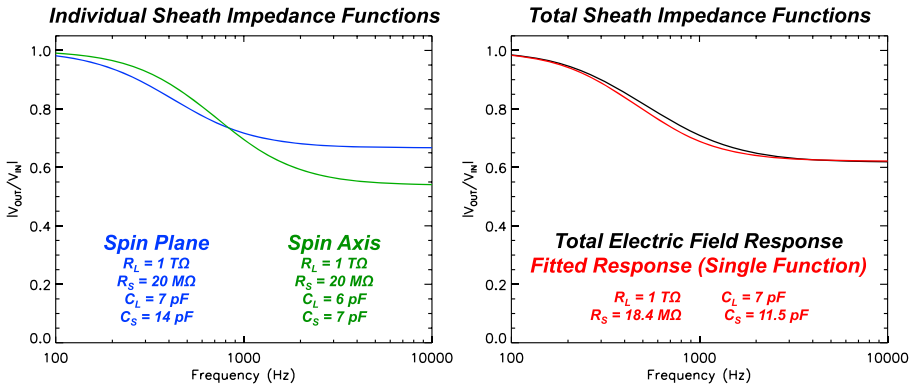

Figure 7. (left) An approximated sheath impedance function for both the spin plane antenna (blue) using R_L = 1 TOhm, R_S = 20 MOhm, C_L = 7 pF, and C_S = 14 pF and for the spin axis antenna (green) using R_L = 1 TOhm, R_S = 20 MOhm, C_L = 6 pF, and C_S = 7 pF. (right) The total electric field sheath impedance function calculated from the individual functions shown in Figure 7 (left) (black)—assuming an equal contribution from each component. A single sheath impedance function (red, R_L = 1 TOhm and C_L = 7 pF) that is fitted to the total electric field sheath impedance function with fitted sheath parameters R_S = 18.4 MOhm and C_S = 11.5 pF.

to the total electric field sheath impedance function by minimizing chi-square (fitted sheath parameters of R_S = 18.4 MOhm and C_S = 11.5 pF). It is evident that the single fitted sheath impedance function (red) is a good representation of the total electric field sheath impedance function calculated from amalgamating the individual antenna functions (black). That is, there is little difference between the red and black lines in Figure 7. Hence, it is justified that a good approximation of the sheath impedance can be obtained by applying only one sheath impedance function to the sum of the outputs from all three antenna.

Assuming the cold plasma dispersion relation yields accurate results on average (as has shown to be the case for plasmaspheric hiss), the sheath impedance function will be related to the ratio of wave amplitudes, which is given by the square root of the wave power ratio. That is, the wave amplitude ratio is essentially the ratio of output to input voltages of the EFW instrument as shown in equation (9), and hence,

$$\left|\frac{V_{\text{out}}}{V_{\text{in}}}\right| = \frac{B_{\text{calc}}}{B_{\text{obs}}} = \frac{E_{\text{obs}}}{E_{\text{calc}}} \tag{10}$$

where E and B are the wave amplitudes of the electric and magnetic field, respectively.

If values of the sheath resistance and sheath capacitance can be found, such that the sheath impedance function accurately describes the average wave amplitude ratios, it is likely that the observed discrepancies can be explained by instrument-plasma coupling effects. This will therefore allow for the sheath effects to be quantified and taken into consideration during future analysis of electric field data from the EFW.

In small intervals of plasma density, the average wave amplitude ratio is considered as a function of frequency. Any frequency/density bins that contain less than 10 points are disregarded. A sheath impedance function is then fitted to these wave amplitude ratios by running a range of sheath resistance and capacitance values (1 MOhm < R_S < 1000 MOhm and 1 pF < C_S < 20 pF) and finding the values that minimize the chi-square statistic. This range of values is based on the expected sheath parameters. The load resistance and capacitance of the EFW probes are held constant at 1 TOhm and 7 pF, respectively. If the number of frequency bins containing data at a specific density is less than five, no fit is performed. If the sheath resistance and capacitance values that minimize chi-square are not at the extremes of the permitted values, and the fit yields a reduced chi-square value less than 0.5, the fits are deemed to reflect the variations observed in the data. Given that the fits are performed to the median wave amplitude ratio, it follows that the error used in the calculation of chi-square is the interquartile range. Figure 8 shows examples of fitted sheath impedance functions that meet the criteria to be deemed a good fit, for a range of different plasma densities. The black line is the median wave amplitude ratio in each frequency bin, with the error bars showing the interquartile range of the wave amplitude ratio distribution. The red line is the fitted sheath impedance function using the sheath resistance and capacitance value that minimize the chi-square statistic. With increasing density (top left to bottom right), the transition frequency (from resistive to capacative coupling) can be seen to increase in frequency in the median wave amplitude ratio data (black line). This is also reflected in the minimized chi-square fits (red line). It is this

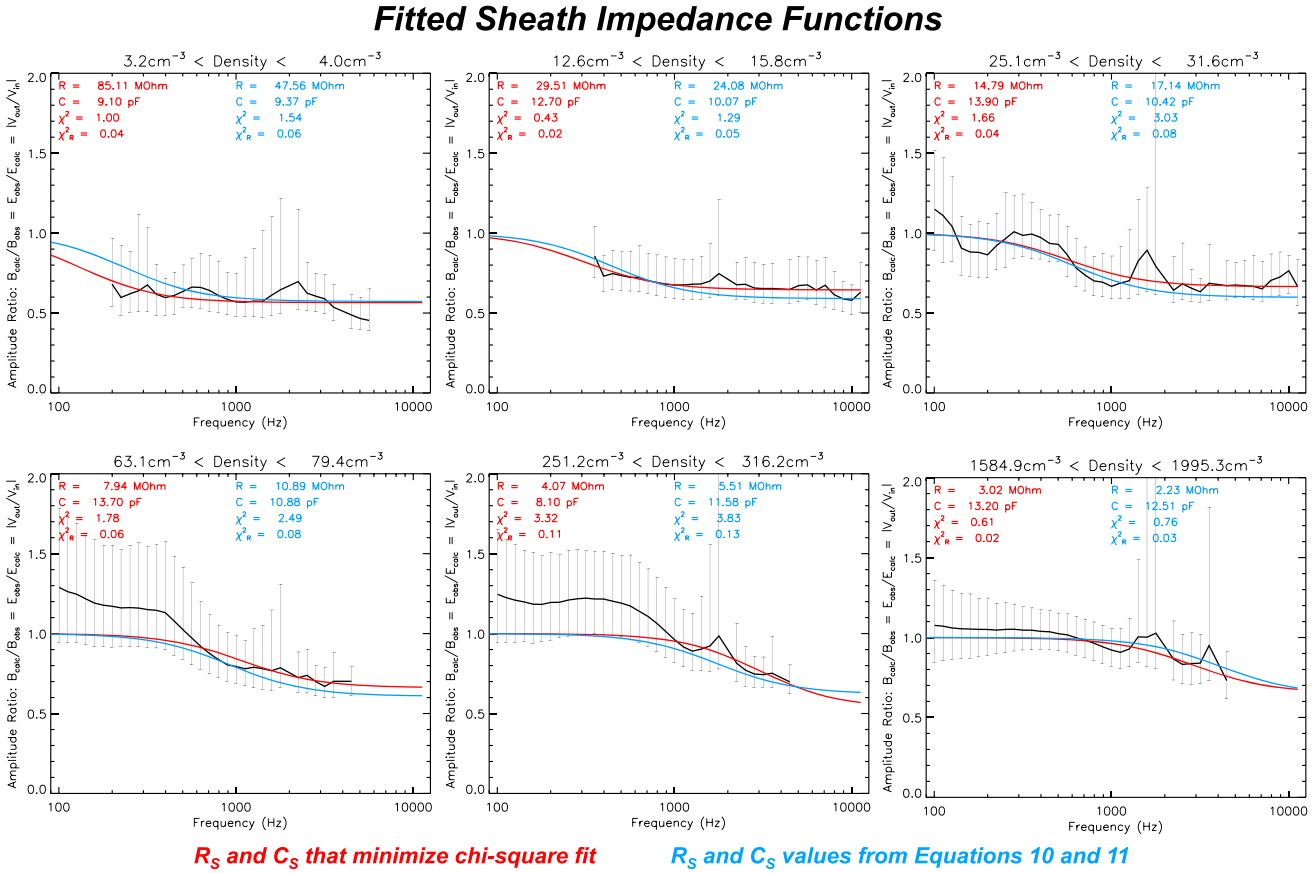

Figure 8. Examples of fitted sheath impedance functions for a range of different plasma densities. The black line is the median wave amplitude ratio (with error bars showing the interquartile range). The red line is the fitted sheath impedance function using the sheath resistance and capacitance value that minimize chi-square. The blue line is the sheath impedance function calculated using the sheath resistance and capacitance values calculated from equations (11) and (12). Also listed on each panel are the resistance and capacitance values used in the fits, as well as the chi-square and minimized chi-square of each fit.

structure that adds weight to the argument that sheath effects are the primary cause of the observed variations. It is worth noting that at higher densities (Figure 8, bottom row), the median wave amplitude ratios at frequencies between 100 and 1000 Hz are greater than one, a feature that this sheath model cannot and does not account for. Overall, Figure 8 shows that the calculated sheath impedance functions are representative of the data across a broad range of plasma densities.

The sheath resistance and capacitance values that yield good fits to the data are then studied as a function of plasma density. It is found that for the majority of the fits, there can be a quite a large degree of variability in both the sheath resistance and sheath capacitance values before the fits are deemed to no longer represent the data. Thus, in order to approximate the effect of instrument-plasma coupling, simple fits are performed to the sheath resistance and capacitance values as a function of plasma density, N. These fits yield equations

$$\log_{10} R_S(\text{MOhm}) = 1.948 - 0.4925 \times \log_{10} N(\text{cm}^{-3}) \tag{11}$$

$$C_S(\text{pF}) = 8.730 + 1.164 \times \log_{10} N(\text{cm}^{-3}) \tag{12}$$

where the load resistance and capacitance are set to R_L = 1 TOhm and C_L = 7 pF, respectively. The form of these fits shows that, as expected, the sheath resistance decreases with increasing density, while the sheath capacitance increases with increasing density. While it is unlikely to be an accurate assertion that the sheath capacitance and the logarithm of the sheath resistance vary linearly with the logarithm of the plasma density, it is believed that these fits do provide a first-order approximation of these values (which is subsequently shown to be the case). The sheath impedance functions that result from using the sheath resistance and capacitance values from equations (11) and (12) are also shown on Figure 8 (blue line). It is evident that

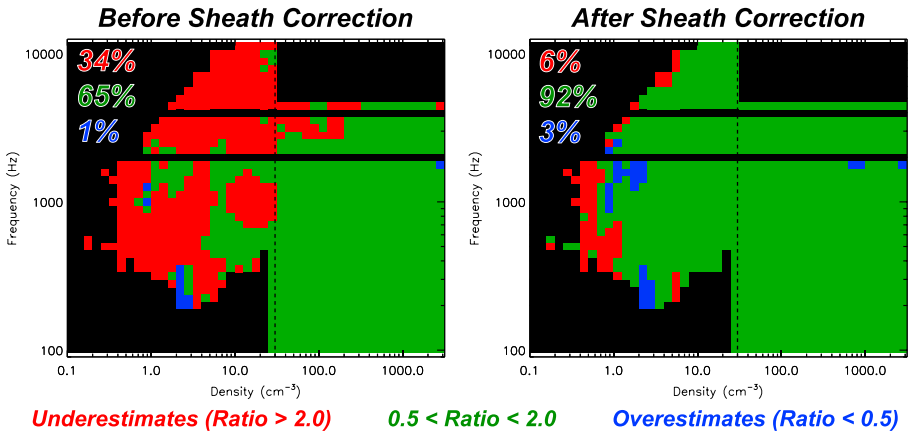

Figure 9. The median of the logarithm of the wave power ratio distribution (observed/calculated) as a function of frequency channel and plasma density binned into discreet ratio bins parametrized as wave power is overestimated by a factor of 2 or greater (Ratio > 0.5), wave power is within a factor of 2 of that observed (0.5 < Ratio < 2.0), and wave power is overestimated by a factor of 2 or greater (Ratio > 2.0). The percentage of bins containing ratios in each of these bands are also listed on the figure. (left) The same data as in Figure 4 (before sheath correction). (right) The wave power ratios once the sheath correction has been applied.

these functions yield values that accurately reflect the sheath impedance function calculated by minimizing chi-square. That is, there is little difference between the red and blue lines in all panels of Figure 8, and hence, these simple equations can provide a good approximation of the sheath parameters.

It is noted that in a very low density plasma, where the Debye length is comparable to the separation of the spherical double probes, the "shorting effect" may occur [e.g., *Pederson et al.*, 1998]. This means that the effective length may no longer be considered to be simply the separation between the spherical double probes of the EFW and is actually some fraction of this length. This may be accounted for by adding an additional fitting parameter (shorting factor), between zero and one, into the sheath impedance function from equation (9). However, due to the comparatively low number of data points and smaller frequency coverage available at very low densities (see Figure 4 (right)), adding in this additional fitting parameter results in large variations of the fitting parameters, with the calculated chi-square values remaining comparable to when the effective length is not considered. Thus, adding an additional fitting parameter is not justified, and hence, the shorting effect is not accounted for in this study.

The calculated plasma sheath effects predicted by equations (11) and (12) are subsequently applied to the data in order to test their accuracy. Note that the calculated sheath impedance functions are not valid for periods where the spin-axis electric field sensor is in shadow, spacecraft eclipse periods, spacecraft charging events, or spacecraft maneuver periods.

6. Applying Sheath Correction

The sheath correction is applied by dividing the calculated magnetic field power spectra by the square of the sheath impedance function shown in equation (9). Figure 9 (left) shows the same parameters as in Figure 4 but with discreet ratio bins parametrized as the wave power is underestimated by a factor of 2 or greater (Ratio > 2.0, red), the wave power is within a factor of 2 of that observed (0.5 < Ratio < 2.0, green), or the wave power is overestimated by a factor of 2 or greater (Ratio < 0.5, blue). The percentage of bins containing ratios in each of these bands are also listed in the figure. Figure 9 (right) shows the wave power ratios once the sheath correction (using the sheath parameters from equations (11) and (12)) has been applied. Prior to the sheath correction (left), 34% of bins contain an underestimate of the average wave power, 65% contain an average calculated wave power that is within a factor of 2 of that observed, and 1% of bins contain an overestimate of the average wave power. Once the sheath correction is applied (right), the percentage of bins containing an underestimate of the average wave power is reduced from 34% to 6%. The number of bins containing an average calculated wave power that is within a factor of 2 of that observed increases from 65% to 92%, with the percentage of overestimates remaining minimal (3%). Tightening the ratio bins to within a factor of 1.5 (instead of 2.0) yields the percentage of bins containing underestimates to be 49% before correction

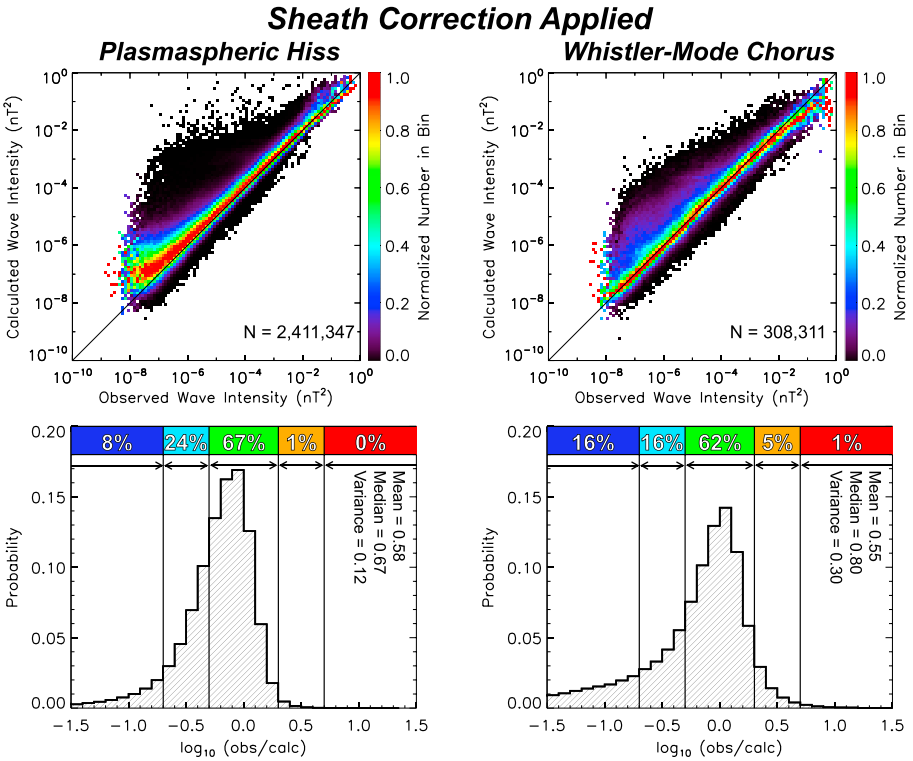

Figure 10. The same parameters as shown in Figures 2 and 3 (including the wave normal angle) once the calculated sheath correction has been applied.

and 9% after correction, the percentage of bins containing values within a factor of 1.5 to be 45% before correction and 75% after correction, and the percentage of bins containing overestimates to be 6% before correction and 16% after correction. These numbers highlight that the sheath correction presented in this study performs well at correcting the average calculated magnetic wave field power spectra. It is noted that the bins containing corrected average wave ratios outside of the 0.5 to 2.0 range typically occur around the edge of the density/frequency ranges where data are available. As such, the number of data points in these bins is typically lower than the number of data points in bins where the corrected calculated power spectra is within a factor of 2 of that observed (see Figure 4). It is also noted that the small collection of corrected average wave power ratios that are overestimated (between ~1 and 3 cm^{-3} in density and ~1000 Hz in frequency) occur in bins where the distribution of ratios is highly skewed, with a long distribution tail reaching out to overestimates. Hence, the median of these distributions is also skewed.

Figure 10 shows the same parameters as in Figures 2 and 3, once the calculated wave powers have been corrected for instrument-plasma coupling effects using sheath parameters calculated from equations (11) and (12) for plasmaspheric hiss (left column) and whistler mode chorus (right column). For plasmaspheric hiss, taking into account the correction due to instrument-plasma coupling has little effect on calculated wave powers with the highest density of data points remaining on, or slightly above, the line of equivalence (Figure 10, top left). The distribution of wave power ratios also remains largely unchanged, with the percentage of data within the defined ratio bands only varying by a few percent. The mean, median, and variance of the ratio distribution also remain relatively unchanged. The peak of the ratio distribution remains centered close to a ratio of unity.

For chorus waves, once the sheath effects are accounted for, the calculated wave powers are much more closely matched to those observed (Figure 10, top right). The systematic underestimates of wave power seen in Figure 3 are no longer observable with the majority of data now lying on the diagonal line of equivalence. It is noted however that at very high wave powers ($B_w^2 > 10^{-2}$ nT^2) the data appear to curve slightly away from the line of equivalence. The distribution of ratios about the line of equivalence once sheath effects have been considered (Figure 10, bottom right) indicates that the peak of the distribution is now centered close to a ratio of unity. The systematic offset, tending toward underestimating wave powers, seen in

Table 1. Summary Percentages of the Accuracy of Calculated Whistler Mode Magnetic Wave Powers for (i) Assuming Parallel Propagation ($\theta = 0°$), (ii) Considering the Wave Normal Angle ($\theta = \theta_k$), and (iii) Considering the Wave Normal Angle and Applying the Sheath Correction Developed in This Study ($\theta = \theta_k$ and Sheath Correction Applied)

Wave Mode	Wave Power Ratio (obs/calc)	$\theta = 0°$	$\theta = \theta_k$	$\theta = \theta_k$ + Sheath Correction
Plasmaspheric hiss	< 0.2	10%	7%	8%
	0.2 < 0.5	26%	23%	24%
	0.5 < 2.0	63%	69%	67%
	2.0 < 5.0	1%	1%	1%
	> 5.0	0%	0%	0%
Whistler mode chorus	< 0.2	37%	9%	16%
	0.2 < 0.5	10%	8%	16%
	0.5 < 2.0	27%	37 %	62%
	2.0 < 5.0	22%	39%	5%
	> 5.0	4%	7%	1%

Figure 3 (bottom right) is no longer a feature. The impact of applying this sheath correction is to increase the percentage of calculated wave powers that are within a factor of 2 of those observed from 37% to 62%. The percentage of wave powers that are underestimated decreases from 46% (39% by a factor greater than 2 but less than 5 and 7% by a factor greater than 5) to only 6% (5% by a factor greater than 2 but less than 5 and 1% by a factor greater than 5), while the percentage of overestimates increases from 17% (8% by a factor greater than 2 but less than 5 and 9% by a factor greater than 5) to 32% (16% by a factor greater than 2 but less than 5 and 16% by a factor greater than 5). The fact that the distribution peak, as well as the median, now sits close to a ratio of unity shows that the applied sheath model performs well at correcting the average wave power, with the remaining scatter attributed to the cold plasma assumption and uncertainties in the inferred plasma frequency.

Overall, the calculated sheath correction is successful in removing the systematic underestimates of the calculated chorus wave powers, bringing them in line with those observed. Additionally, the calculated plasmaspheric hiss wave powers are not significantly affected by this correction—an important result given the high level of agreement prior to considering sheath effects. It is worth noting that this analysis is reliant on the cold plasma assumption remaining valid, even in a plasma that contains a significant warm/hot component (e.g., outside of the plasmasphere). However, given the similarity in structure between what is observed and what is expected due to instrument-plasma coupling, it is deemed reasonable that the primary cause of the observed discrepancies is due to sheath effects, and not the assumption of a cold plasma regime. Hence, these results show that the variation of the ratio of calculated to observed wave powers is not only consistent with but can be successfully explained by instrument-plasma coupling effects and indeed corrected for.

Table 1 provides summary percentages of the accuracy of calculated whistler mode magnetic wave powers for (i) assuming parallel propagation ($\theta = 0°$), (ii) considering the wave normal angle ($\theta = \theta_k$), and (iii) considering the wave normal angle and applying the sheath correction developed in this study ($\theta = \theta_k$ and Sheath Correction Applied).

The accuracy of the calculated sheath impedance functions have been thoroughly tested for whistler mode waves. However, in actuality, all EFW wave electric field measurements are subject to instrument-plasma coupling effects. Hence, the sheath impedance functions calculated in this study may be applied to all EFW wave data, regardless of wave mode. However, it is noted that the accuracy of the sheath impedance correction presented in this study is difficult to determine for waves not in the whistler mode. Additionally, the methodology of this study may be used to quantify the variable antenna-sheath impedance for electric field instruments on board other spacecraft where both the wave electric field and wave magnetic field measurements are available.

7. Conclusions

Including the wave normal angle from EMFISIS in the calculation of whistler mode magnetic field wave powers from electric field power spectra: (1) Does not significantly impact the calculated wave powers for plasmaspheric hiss—assumption of parallel propagation is valid. (2) Significantly reduces the number of overestimates (by a factor of 2 or greater) of chorus wave powers from 47% to 17% (particularly evident between observed wave powers of 10^{-7} and 10^{-4} nT^2). (3) Does not explain, and actually increases, the percentage of underestimates of chorus wave power (systematic offset).

The variations in wave power ratios expected from instrument-plasma coupling via the formation of a plasma sheath around the EFW probes (as a function of plasma density and measured frequency channels) are consistent with what is observed. By using the cold plasma dispersion relation and including the wave normal angle, the effect of instrument-plasma coupling has been quantified by using simple, density-dependent functions (equations (11) and (12)). Using these calculated functions to correct for sheath effects: (1) Increases the percentage of densities/frequencies where the average wave power is within a factor of 2 of that observed from 65% to 92%, and within a factor of 1.5 of that observed from 45% to 75%. (2) Removes the systematic underestimates of chorus wave powers, bringing calculated wave powers in line with those observed. The percentage of calculated wave powers that are within a factor of 2 of those observed is increased from 37% to 62%. (3) Successfully corrects the underestimates of power spectra and wave power.

This study takes the first step toward determining the correct theoretical treatment of whistler mode waves in the magnetosphere by quantifying the accuracy of both the cold plasma assumption and the assumption of parallel wave propagation. Due to the structure of the discrepancies between calculated and observed whistler mode wave powers that remain once the assumption of parallel propagation is removed, it is concluded that instrument-plasma coupling effects with EFW instrumentation are the primary cause of these deviations. A simple, density-dependent model has been developed in order to quantify these effects that have shown to successfully correct both calculated power spectra and wave powers in the whistler mode. However, the calculated sheath impedance functions are not just limited to whistler mode waves—they may be applied to all EFW wave data, regardless of the wave mode.

The methodology of this study may also be repeated to determine the variable antenna-sheath impedance for other spacecraft missions where both wave electric field and wave magnetic field measurements are available.

Acknowledgments
This work was performed under the support of JHU/APL contract 921647 under NASA Prime contract NAS5-01072. Van Allen Probes EMFISIS data are available at http://emfisis.physics.uiowa.edu/data/index. O.S. acknowledges support from grants LH14010, LH15304, and Praemium Academiae. C.E.J.W. is supported by STFC grant ST/M000885/1. The authors would like to acknowledge Yue Chen for his part in initial investigations with this research.

References

Boehm, M. H., C. W. Carlson, J. P. McFadden, J. H. Clemmons, R. E. Ergun, and F. S. Mozer (1994), Wave rectification in plasma sheaths surrounding electric field antennas, *J. Geophys. Res.*, *99*(A11), 21,361–21,374, doi:10.1029/94JA01766.

Burtis, W. J., and R. A. Helliwell (1969), Banded chorus—A new type of VLF radiation observed in the magnetosphere by OGO 1 and OGO 3, *J. Geophys. Res.*, *74*(11), 3002–3010, doi:10.1029/JA074i011p03002.

Chen, Y., G. D. Reeves, and R. H. Friedel (2007), The energization of relativistic electrons in the outer Van Allen radiation belt, *Nat. Phys.*, *3*, 614–617, doi:10.1038/nphys655.

Fu, X., Z. Guo, C. Dong, and S. P. Gary (2015), Nonlinear subcyclotron resonance as a formation mechanism for gaps in banded chorus, *Geophys. Res. Lett.*, *42*, 3150–3159, doi:10.1002/2015GL064182.

Gurnett, D. A. (1998), Principles of space plasma wave instrument design, in *Measurement Techniques in Space Plasmas Fields*, edited by R. F. Pfaff, J. E. Borovsky, and D. T. Young, p. 121, AGU, Washington, D. C., doi:10.1002/9781118664391.ch14.

Green, J. C., and M. G. Kivelson (2004), Relativistic electrons in the outer radiation belt: Differentiating between acceleration mechanisms, *J. Geophys. Res.*, *109*, A03213, doi:10.1029/2003JA010153.

Green, J. C., T. G. Onsager, T. P. OBrien, and D. N. Baker (2004), Testing loss mechanisms capable of rapidly depleting relativistic electron flux in the Earth's outer radiation belt, *J. Geophys. Res.*, *109*, A12211, doi:10.1029/2004JA010579.

Hartley, D. P., M. H. Denton, J. C. Green, T. G. Onsager, J. V. Rodriguez, and H. J. Singer (2013), Case studies of the impact of high-speed solar wind streams on the electron radiation belt at geosynchronous orbit: Flux, magnetic field, and phase space density, *J. Geophys. Res. Space Physics*, *118*, 6964–6979, doi:10.1002/2013JA018923.

Hartley, D. P., M. H. Denton, and J. V. Rodriguez (2014), Electron number density, temperature, and energy density at GEO and links to the solar wind: A simple predictive capability, *J. Geophys. Res. Space Physics*, *119*, 4556–4571, doi:10.1002/2014JA019779.

Hartley, D. P., Y. Chen, C. A. Kletzing, M. H. Denton, and W. S. Kurth (2015), Applying the cold plasma dispersion relation to whistler mode chorus waves: EMFISIS wave measurements from the Van Allen Probes, *J. Geophys. Res. Space Physics*, *120*, 1144–1152, doi:10.1002/2014JA020808.

Horne, R. B., and R. M. Thorne (1998), Potential waves for relativistic electron scattering and stochastic acceleration during magnetic storms, *Geophys. Res. Lett.*, *25*(15), 3011–3014, doi:10.1029/98GL01002.

Horne, R. B., R. M. Thorne, S. A. Glauert, J. M. Albert, N. P. Meredith, and R. R. Anderson (2005), Timescale for radiation belt electron acceleration by whistler mode chorus waves, *J. Geophys. Res.*, *110*, A03225, doi:10.1029/2004JA010811.

Kennel, C. F., and F. Engelmann (1966), Velocity space diffusion from weak plasma turbulence in a magnetic field physics of fluids, *9*, 2377–2388, doi:10.1063/1.1761629.

Kletzing, C. A. (2013), The Electric and Magnetic Field Instrument Suite and Integrated Science (EMFISIS) on RBSP, *Space Sci. Rev.*, *179*, 127–181, doi:10.1007/s11214-013-9993-6.

Kurth, W. S., S. De Pascuale, J. B. Faden, C. A. Kletzing, G. B. Hospodarsky, S. Thaller, and J. R. Wygant (2015), Electron densities inferred from plasma wave spectra obtained by the Waves instrument on Van Allen Probes, *J. Geophys. Res. Space Physics*, *120*, 904–914, doi:10.1002/2014JA020857.

Lam, M. M., R. B. Horne, N. P. Meredith, and S. A. Glauert (2007), Modeling the effects of radial diffusion and plasmaspheric hiss on outer radiation belt electrons, *Geophys. Res. Lett.*, *34*, L20112, doi:10.1029/2007GL031598.

Li, W., et al. (2013), Characteristics of the Poynting flux and wave normal vectors of whistler-mode waves observed on THEMIS, *J. Geophys. Res. Space Physics*, *118*, 1461–1471, doi:10.1002/jgra.50176.

Li, W., et al. (2014), Evidence of stronger pitch angle scattering loss caused by oblique whistler-mode waves as compared with quasi-parallel waves, *Geophys. Res. Lett.*, *41*, 6063–6070, doi:10.1002/2014GL061260.

Lyons, L. R., R. M. Thorne, and C. F. Kennel (1972), Pitch-angle diffusion of radiation belt electrons within the plasmasphere, *J. Geophys. Res.*, *77*(19), 3455–3474, doi:10.1029/JA077i019p03455.

Lyons, L. R., and R. M. Thorne (1973), Equilibrium structure of radiation belt electrons, *J. Geophys. Res.*, *78*(13), 2142–2149, doi:10.1029/JA078i013p02142.

Meredith, N. P., R. B. Horne, R. M. Thorne, and R. R. Anderson (2003a), Favored regions for chorus-driven electron acceleration to relativistic energies in the Earth's outer radiation belt, *Geophys. Res. Lett.*, *30*(16), 1871, doi:10.1029/2003GL017698.

Meredith, N. P., M. Cain, R. B. Horne, R. M. Thorne, D. Summers, and R. R. Anderson (2003b), Evidence for chorus-driven electron acceleration to relativistic energies from a survey of geomagnetically disturbed periods, *J. Geophys. Res.*, *108*(A6), 1248, doi:10.1029/2002JA009764.

Meredith, N. P., R. B. Horne, R. M. Thorne, D. Summers, and R. R. Anderson (2004), Substorm dependence of plasmaspheric hiss, *J. Geophys. Res.*, *109*, A06209, doi:10.1029/2004JA010387.

Meredith, N. P., R. B. Horne, S. A. Glauert, and R. R. Anderson (2007), Slot region electron loss timescales due to plasmaspheric hiss and lightning-generated whistlers, *J. Geophys. Res.*, *112*, A08214, doi:10.1029/2007JA012413.

Meredith, N. P., R. B. Thorne, A. Sicard-Piet, D. Boscher, K. H. Yearby, W. Li, and R. M. Thorne (2012), Global model of lower band and upper band chorus from multiple satellite observations, *J. Geophys. Res.*, *117*, A10225, doi:10.1029/2012JA017978.

Morley, S. K., R. H. W. Friedel, E. L. Spanswick, G. D. Reeves, J. T. Steinberg, J. Koller, T. Cayton, and E. Noveroske (2010), Dropouts of the outer electron radiation belt in response to solar wind stream interfaces: Global positioning system observations, *Proc. R. Soc. A*, *466*, 3329–3350, doi:10.1098/rspa.2010.0078.

Ni, B., R. M. Thorne, N. P. Meredith, Y. Y. Shprits, and R. B. Horne (2011), Diffuse auroral scattering by whistler mode chorus waves: Dependence on wave normal angle distribution, *J. Geophys. Res.*, *116*, A10207, doi:10.1029/2011JA016517.

Onsager, T. G., et al. (2002), Radiation belt electron flux dropouts: Local time, radial, and particle-energy dependence, *J. Geophys. Res.*, *107*(A11), 1382, doi:10.1029/2001JA000187.

Pederson, A., F. Mozer, and G. Gustafsson (1998), Electric field measurements in a tenuous plasma with spherical double probes, in *Measurement Techniques in Space Plasmas: Fields, Geophys. Monogr. Ser.*, vol. 103, p. 1, AGU, Washington, D. C.

Reeves, G. D., K. L. McAdams, R. H. W. Friedel, and T. P. O'Brien (2003), Acceleration and loss of relativistic electrons during geomagnetic storms, *Geophys. Res. Lett.*, *30*(10), 1529, doi:10.1029/2002GL016513.

Reeves, G. D., et al. (2013), Electron acceleration in the heart of the Van Allen radiation belts, *Science*, *341*, 991–994, doi:10.1126/science.1237743.

Santolík, O., J. S. Pickett, D. A. Gurnett, and L. R. O. Storey (2002), Magnetic component of narrowband ion cyclotron waves in the auroral zone, *J. Geophys. Res.*, *107*(A12), 1444, doi:10.1029/2001JA000146.

Santolík, O., M. Parrot, and F. Lefeuvre (2003), Singular value decomposition methods for wave propagation analysis, *Radio Sci.*, *38*, 1010, doi:10.1029/2000RS002523.

Santolik, O., D. A. Gurnett, J. S. Pickett, J. Chum, and N. Cornilleau-Wehrlin (2009), Oblique propagation of whistler mode waves in the chorus source region, *J. Geophys. Res.*, *114*, A00F03, doi:10.1029/2009JA014586.

Santolík, O., C. A. Kletzing, W. S. Kurth, G. B. Hospodarsky, and S. R. Bounds (2014a), Fine structure of large-amplitude chorus wave packets, *Geophys. Res. Lett.*, *41*, 293–299, doi:10.1002/2013GL058889.

Santolík, O., E. Macúsová, I. Kolmašová, N. Cornilleau-Wehrlin, and Y. de Conchy (2014b), Propagation of lower-band whistler-mode waves in the outer Van Allen belt: Systematic analysis of 11 years of multi-component data from the Cluster spacecraft, *Geophys. Res. Lett.*, *41*, 2729–2737, doi:10.1002/ 2014GL059815.

Shprits, Y., M. Daae, and B. Ni (2012), Statistical analysis of phase space density buildups and dropouts, *J. Geophys. Res.*, *117*, A01219, doi:10.1029/2011JA016939.

Stix, T. H. (1992), *Waves in Plasmas*, Am. Inst. Phys.

Summers, D., and C. Ma (2000), A model for generating relativistic electrons in the Earth's inner magnetosphere based on gyroresonant wave-particle interactions, *J. Geophys. Res.*, *105*(A2), 2625–2639, doi:10.1029/1999JA900444.

Summers, D., R. M. Thorne, and F. Xiao (1998), Relativistic theory of wave-particle resonant diffusion with application to electron acceleration in the magnetosphere, *J. Geophys. Res.*, *103*(A9), 20,487–20,500, doi:10.1029/98JA01740.

Summers, D., C. Ma, N. P. Meredith, R. B. Horne, R. M. Thorne, D. Heynderickx, and R. R. Anderson (2002), Model of the energization of outer-zone electrons by whistler-mode chorus during the October 9, 1990 geomagnetic storm, *Geophys. Res. Lett.*, *29*(24), 2174, doi:10.1029/2002GL016039.

Summers, D., B. Ni, and N. P. Meredith (2007), Timescales for radiation belt electron acceleration and loss due to resonant wave-particle interactions: 2. Evaluation for VLF chorus, ELF hiss, and electromagnetic ion cyclotron waves, *J. Geophys. Res.*, *112*, A04207, doi:10.1029/2006JA011993.

Summers, D., B. Ni, N. P. Meredith, R. B. Horne, R. M. Thorne, M. B. Moldwin, and R. R. Anderson (2008), Electron scattering by whistler-mode ELF hiss in plasmaspheric plumes, *J. Geophys. Res.*, *113*, A04219, doi:10.1029/2007JA012678.

Thorne, R. M. (2010), Radiation belt dynamics: The importance of wave-particle interactions, *Geophys. Res. Lett.*, *37*, L22107, doi:10.1029/2010GL044990.

Thorne, R. M., et al. (2013), Evolution and slow decay of an unusual narrow ring of relativistic electrons near L∼3.2 following the September 2012 magnetic storm, *Geophys. Res. Lett.*, *40*, 3507–3511, doi:10.1002/grl.50627.

Tsurutani, B. T., and E. J. Smith (1974), Postmidnight chorus: A substorm phenomenon, *J. Geophys. Res.*, *79*(1), 118–127, doi:10.1029/JA079i001p00118.

Tsurutani, B. T., and E. J. Smith (1977), Two types of magnetospheric ELF chorus and their substorm dependences, *J. Geophys. Res.*, *82*(32), 5112–5128, doi:10.1029/JA082i032p05112.

Turner, D. L., X. Li, G. D. Reeves, and H. J. Singer (2010), On phase space density radial gradients of Earth's outer-belt electrons prior to sudden solar wind pressure enhancements: Results from distinctive events and a superposed epoch analysis, *J. Geophys. Res.*, *115*, A01205, doi:10.1029/2009JA014423.

Turner, D. L., et al. (2012), Explaining sudden losses of outer radiation belt electrons during geomagnetic storms, *Nat. Phys.*, *8*, 208–212, doi:10.1038/nphys2185.

Watt, C. E. J., R. Rankin, and A. W. Degeling (2012), Whistler mode wave growth and propagation in the prenoon magnetosphere, *J. Geophys. Res.*, *117*, A06205, doi:10.1029/2012JA017765.

Wygant, J. R., et al. (2013), The Electric Field and Waves (EFW) instruments on the radiation belt storm probes mission, *Space Sci. Rev.*, *179*, 183–220, doi:10.1007/s1124-013-0013-7.